Hindawi
International Journal of Photoenergy
Volume 2022, Article ID 1172871, 11 pages
https://doi.org/10.1155/2022/1172871

Research Article

Controlled Crystallinity of TiO_2 Layers Grown by Atmospheric Pressure Spatial Atomic Layer Deposition and their Impact on Perovskite Solar Cell Efficiency

Eugen Zimmermann,[1] Ka Kan Wong,[1] Tobias Seewald,[1] Julian Kalb,[1] Jonathan Steffens,[2] Giso Hahn,[2] and Lukas Schmidt-Mende[1]

[1]*Hybrid-Nanostructures, University of Konstanz, 78457 Konstanz, Germany*
[2]*Photovolatics Division, University of Konstanz, 78457 Konstanz, Germany*

Correspondence should be addressed to Lukas Schmidt-Mende; lukas.schmidt-mende@uni-konstanz.de

Received 29 June 2022; Accepted 13 September 2022; Published 30 September 2022

Academic Editor: Chaofan Sun

Atmospheric Pressure Spatial Atomic Layer Deposition (AP-SALD) is an upcoming deposition technique suitable for a variety of materials and combines the benefits of a regular atomic layer deposition with a significantly increased deposition rate at ambient conditions. In this work, amorphous and anatase TiO_2 layers are fabricated by AP-SALD via systematic variation of process conditions such as temperature, reactant (H_2O and O_3), and posttreatment. The formed layers are characterized for their structural and optoelectronic properties and utilized as a hole-blocking layer in hybrid perovskite solar cells. It is found that TiO_2 layers fabricated at elevated deposition temperatures possess strong anatase character but expose an unfavorable interface to the perovskite layer, promoting recombination and lowering the shunt resistance and open circuit voltage of the solar cells. Therefore, the interface is essential for efficient charge extraction, which can be significantly improved by controlling the process parameters.

1. Introduction

TiO_2 is an earth-abundant and very versatile material used in many optoelectronic and electronic applications like water splitting [1], gas sensing [2, 3], transistors [4–6], and solar cells. Its n-type character, an optical bandgap of about 3.0, 3.2, or 3.5 eV for rutile, anatase, and amorphous morphology, respectively, and its suitable energetic landscape have made it a commonly used electron selective layer in solar cells for almost 30 years [7–9]. During this time, many fabrication techniques for thin film and nanostructured layers have been developed, including spray pyrolysis [10–12], sputter deposition [13], electron-beam evaporation [14], chemical vapour deposition [15], sol-gel process [16–18], electrodeposition [19, 20], hydrothermal growth [21, 22], and atomic layer deposition (ALD) [23–26]. Thereby, ALD is of particular interest, as it allows the reproducible fabrication of pin-hole free layers of high quality on flat films and conformal coatings on nanostructures. Additionally, the resulting layer properties, like thickness and crystallinity, are precisely adjustable by the processing conditions such as temperature, pressure, purge, and exposure time as well as by the choice of precursor and reactant. Typically, $TiCl_4$, titanium tetraisopropoxide (TTIP), and tetrakis dimethylamino titanium are used as precursors and H_2O, H_2O_2, and O_3 as reactant. Spatial atomic layer deposition at atmospheric pressure (AP-SALD) is the next evolutionary step of ALD and extends the precise thickness control of ALD by a fast vacuum free and upscalable deposition in ambient environment [27, 28].

Here, we demonstrate the controlled fabrication of amorphous and anatase TiO_2 by AP-SALD and relate the

Table 1: Summary of measured and modeled structural and optical properties.

	Temperature (°C)	AFM RMS (nm)	SE model Roughness (nm)	SE model Thickness (nm)	SE model GPC (nm/cycle)	SE model MSE	SE model n (530)	UV-Vis E_{gap} (eV)	KP WF (eV)	UPS WF (eV)	UPS VBM (eV)
H_2O	100	1.2	1.7	89.9	0.09	0.7	2.07	3.53	-4.58	-4.54	-7.41
	150	0.9	1.9	82.4	0.08	0.6	2.19	3.53	-4.58	-4.72	-7.51
	200	1.1	2.9	84.4	0.08	0.6	2.37	3.51	-4.65	-4.54	-7.26
	250	10.0	7.5	105	0.11	3.8	2.54	3.49	-4.65	-4.74	-7.46
	300	8.5	11.9	114.5	0.11	3.9	2.53	3.45	-4.70	-4.73	-7.46
	350	11.2	11.6	111.7	0.11	4.5	2.54	3.36	-4.70	-4.76	-7.55
O_3	100	—	2	89.5	0.09	1.2	2.07	3.49	-4.59	-4.73	-7.59
	150	0.8	1.7	75.6	0.08	1.1	2.21	3.50	-4.47	-4.72	-7.52
	200	1.0	1.6	53.3	0.05	0.7	2.40	3.45	-4.48	-4.71	-7.40
	250	2.3	1.9	59.4	0.06	1.6	2.56	3.34	-4.70	-4.70	-7.38
	300	12.6	3.1	89.4	0.09	6.0	2.55	3.43	-4.62	-4.77	-7.54
	350	13.9	5.1	86.1	0.09	6.2	2.57	3.30	-4.67	-4.77	-7.46

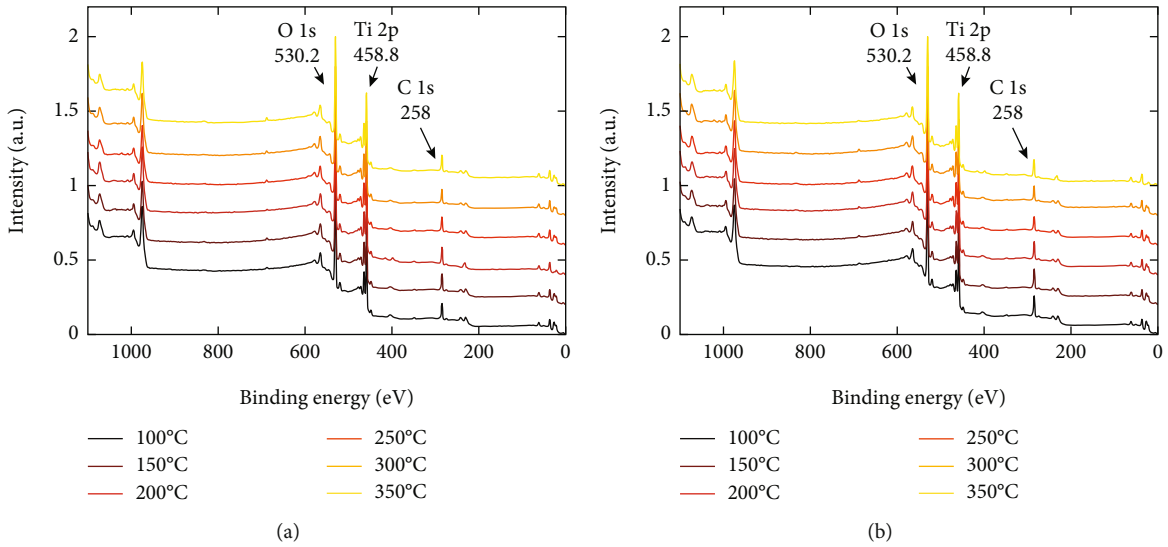

Figure 1: XPS overview scans of TiO_2 with (a) H_2O and (b) O_3 as reactant at varying deposition temperatures and 1000 deposition cycles.

influence of processing parameters to structural, optical, and electronic properties and their implication on the performance of perovskite solar cells.

2. Methods

2.1. TiO_2 Layer Preparation. TiO_2 layers were fabricated on a homemade AP-SALD system with one precursor and one reactant line, and three curtain lines, each with an outlet area of 3.5 mm^2. TTIP (>97%, Sigma Aldrich) was used as metal source precursor and H_2O or O_3 as reactant. In order to avoid condensation, the titanium precursor, transport tubes, and deposition head were preheated to 85°C. Bubble flow rate for N_2 was set to 150 Nml/min for TTIP and 100 Nml/min for H_2O. Flow rate of the N_2 transport gas stream was set to 300 Nml/min in both cases, whereas the flow rate of the N_2 curtain line was set to 600 Nml/min. O_3 flow rate, with oxygen as transport gas, was manually adjusted in line with the H_2O flow rate. Substrates were held on a heated stage by vacuum and passed the deposition head twice for one cycle. The distance between deposition head and substrate was adjusted to about 250 μm. For layer fabrication with an incorporated temperature gradient, the first layer was deposited at the initial temperature which then was smoothly increased/decreased until the final temperature was reached.

Layers for Raman spectroscopy and profilometer measurements were fabricated on microscope glass slides. Layers for atomic force microscopy (AFM), scanning electron microscopy (SEM), energy-dispersive X-ray spectroscopy (EDX), spectroscopic ellipsometry (SE), X-ray and ultraviolet photoelectron spectroscopy (XPS and UPS), and Kelvin probe (KP) were fabricated on polished silicon (111, n-type, Active Business Company GmbH) wafers, and for ultraviolet–

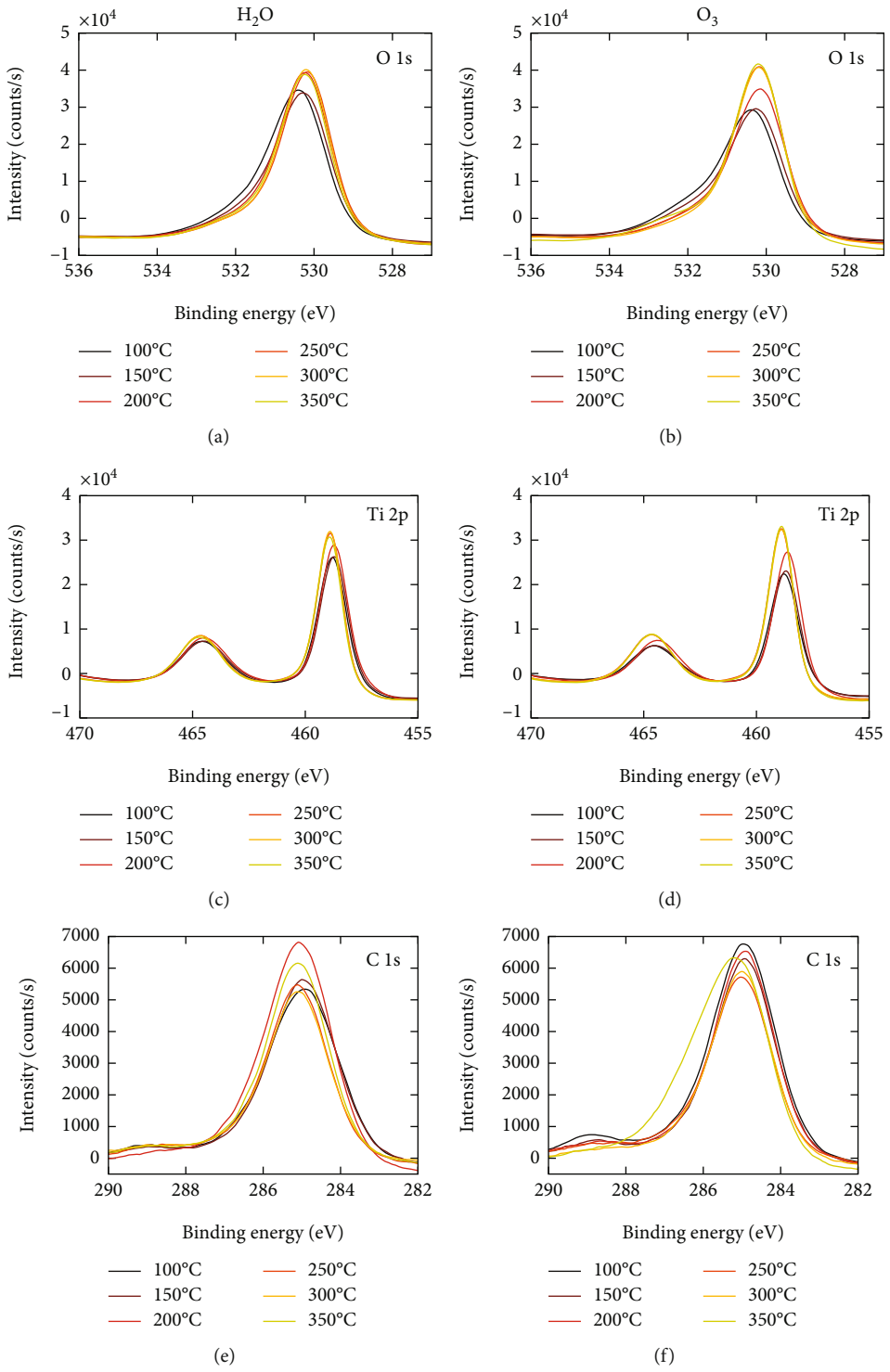

FIGURE 2: XPS detailed scans of Ti 2p, O 1s, and C 1s of TiO_2 samples with (a, c, e) H_2O and (b, d, f) O_3 as reactant at varying deposition temperatures and 1000 deposition cycles.

visible spectroscopy (UV-Vis) and solar cells on tin-doped indium oxide (ITO, <15 Ω/□, Luminescence Technology Corp.). Layers for Transmission Electron Microscopy (TEM) and selected area diffraction (SAD) were directly fabricated on 75 nm Si_3N_4 (S171-3, Agar Scientific) membranes. Sample thickness has been varied in terms of deposition cycles: 2000 cycles for Raman spectroscopy, 75 and 1000 cycles for UPS/XPS, 500 to 2000 cycles for thickness calibration by ellipsometry, 800 cycles for TEM and SAD, and 1000 cycles for all other measurements.

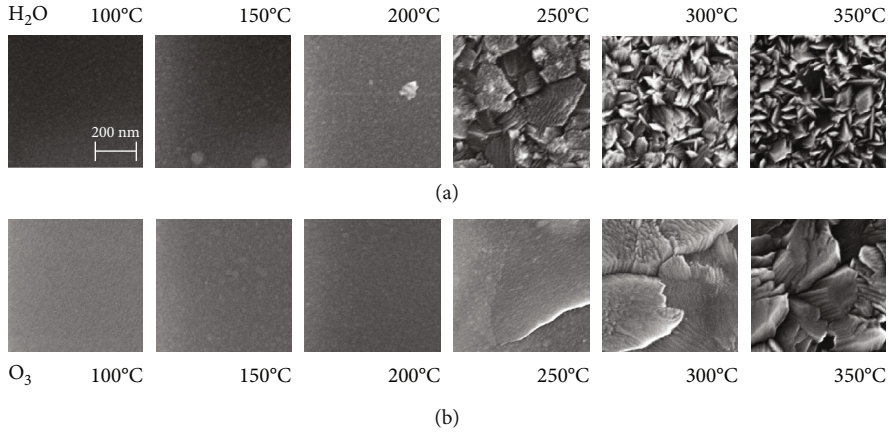

Figure 3: SEM images of TiO_2 layers on Si fabricated between 100°C and 350°C with H_2O (a) and O_3 (b) as reactant and 1000 deposition cycles.

Layers for XPS and UPS have been used as fabricated without cleaning or sputtering to exclude change in atomic composition and bindings.

As reference, a~70 nm thick TiO_2 layer was deposited by spin-casting a commercial sol-gel paste (Ti-Nanoxide BL/SC, Solaronix) and sintered at 450°C for 30 minutes.

2.2. Perovskite Solar Cell Preparation. The perovskite solar cells (MAPbI, $CH_3NH_3PbI_3$) were fabricated via a two-step deposition method. All chemicals were used as purchased without further purification. ITO coated glass substrates were ultrasonically cleaned for 5 min in detergent, acetone, and isopropanol consecutively, followed by N_2 drying. Subsequently, a TiO_2 blocking layer was deposited on the substrates either by AP-SALD or via the sol-gel process as reference. In case of modification by [6,6]-phenyl-C61-butyric acid (PCBA, Solenne BV), the substrates were emerged into a PCBA bath (0.2 mM in chloroform) for 1 hour. They were then transferred to a glove-box where moisture and oxygen levels were kept below 5 ppm. PbI_2 solution (1 M in anhydrous dimethylformamide) and substrates were preheated and maintained at 60°C before spin-coating. Hot PbI_2 solution was spin-cast on the substrates at 5000 rpm for 15 s, which were then quickly transferred onto a hotplate at 70°C for drying. Subsequently, substrates were drop-coated with 6.54 w/v % methylammonium iodide (Solaronix) in anhydrous isopropanol for 20 s, spun at 4000 rpm for 20 s, and annealed at 100°C for 10 min. Spiro-OMeTAD (80 mg/ml, Merck) was spin-cast at 4000 rpm for 120 s, and WO_3 (3 nm)/Ag (100 nm) were finally deposited on top by thermal evaporation.

3. Results

To aim for high quality TiO_2 thin films and their desired application in solar cells, we comprehensively investigated the role of varying deposition parameters on layer formation, crystallinity, and interfacial effects. Therefore, we systematically varied the deposition temperature and the reactant (H_2O and O_3) during the AP-SALD process and analyzed the resulting structural and optoelectronic properties, as well as basic solar cell characteristics.

3.1. Structural Analysis. The layers for structural analysis were fabricated at sample temperatures between 100 and 400°C with a fixed number of cycles underneath the deposition head. The resulting thickness was determined by profilometer measurements and spectroscopic ellipsometry, yielding a growth per cycle (GPC) rate of about 0.7-1 Å/cycle for H_2O and slightly lower for O_3 as reactant (see Table 1 and Figure S1 in SI).

XPS measurements of thin (75 cycles~6 nm) and thick (1000 cycles~80 nm) layers confirm that samples at all temperatures consist of TiO_2 with comparable carbon contamination of the surface determined by the C 1s peak at 285 eV. The major titanium peak Ti $2p_{3/2}$ is detected at a binding energy of 458.8 eV and can be assigned to an oxidation state of Ti^{4+}, whereas the corresponding O 1s signal is in accordance shifted to 530.3 eV (see Figures 1 and 2 as well as Figure S2 to S4 in the SI) [29–31]. Deconvolution of the O 1s peak into an Ti^{4+} (530.4 eV) and an Ti^{3+} (532 eV) contribution, the Ti^{3+} content is notably decreasing with increasing temperature, indicating a reduction of defects for both reactants [32, 33].

SEM images of investigated layers for sample temperatures between 100 and 350°C are shown in Figure 3 (more details in Figure S5 to S16 in the SI). For H_2O as reactant, deposited layers start to crystallize in the anatase phase at sample temperatures of 200°C. Thereby, an amorphous layer is formed prior to nucleation of small anatase crystallites, which is also evident from the transmission electron microscopy and the selected area electron diffraction of the corresponding regions shown in Figure 4. As temperature increases above 250°C, the crystallization process is strongly enhanced and crystallites with preferential growth orientation are formed. First, the crystal growth is leading to flat terrace-like grains with sizes of 200 to 300 nm. For further increased temperatures, the crystal shape is changing to a plate-like structure with dimensions of about 100 nm. A similar crystallization process was described for $TiCl_4$ as Ti-precursor in regular ALD systems [23, 34, 35] and recently was also

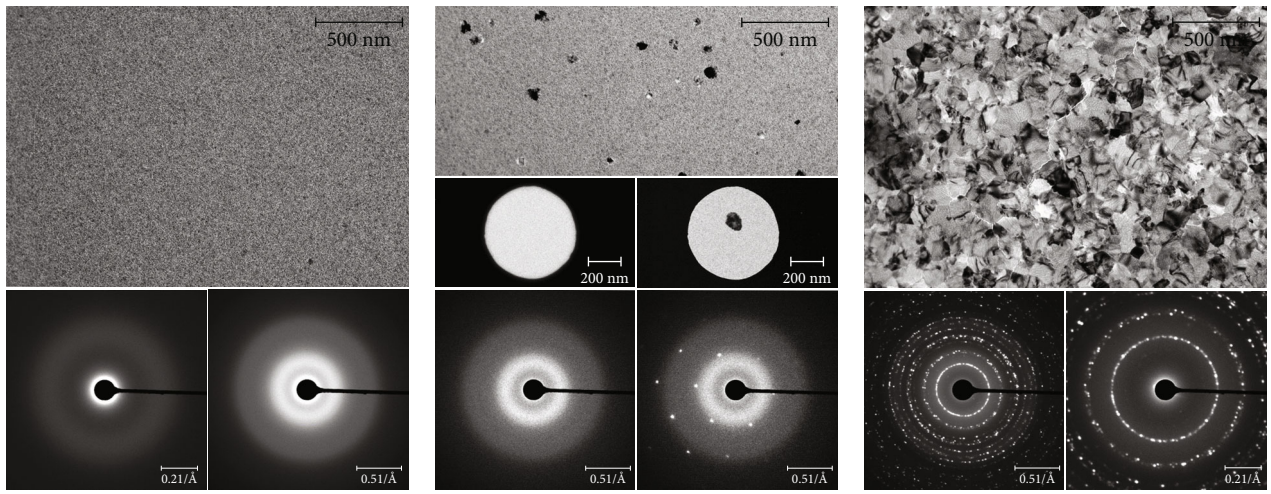

FIGURE 4: TEM and SAD images of TiO_2 layers fabricated with H_2O as reactant at deposition temperatures of (a) 100, (b) 200, and (c) 300°C and 800 deposition cycles.

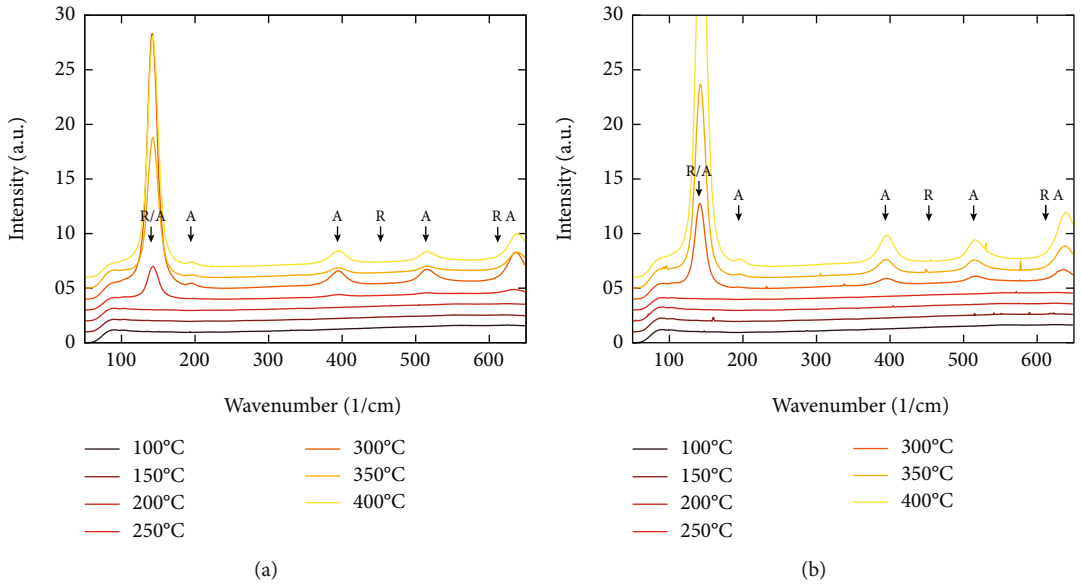

FIGURE 5: Raman spectra of fabricated TiO_2 layers for (a) H_2O and (b) O_3 as reactant and 2000 deposition cycles. Layers are analyzed for anatase (A) and rutile (R) crystal structure. Distinct signals for anatase are observed for temperatures of at least 250°C and 300°C for H_2O and O_3 as reactant, respectively.

described for TTIP and H_2O in another AP-SALD system [36], though with a slightly different temperature onset for crystallization of anatase layers.

With O_3 as reactant, the crystallization process starts at higher temperatures and leads to significantly larger grain sizes of more than 1 μm. As in case of H_2O, the grain-size decreases with increasing temperatures, but the terrace-like facets remain more discernable. The structural change combined with the temperature-dependent variation in growth rate suggest a transition from a space-limited (due to a small amount of nucleation sites) to a general crystal growth with increasing temperature, superimposed by Ostwald ripening at intermediate and decomposition of the precursor at elevated temperatures [34, 36, 37]. Furthermore, for both reactants this transition is associated with a change in surface roughness, which is increasing from about 1 to 10 nm root mean square (RMS). This is evident from AFM (see Figure S17 in the SI) measurements and consistent with fit parameters extracted from the utilized SE model (compare Table 1). The different results between H_2O and O_3 in terms of morphology and growth rate are attributed to a different chemisorption of the incoming TTIP precursor and the respective surface reaction mechanism, as well as the resulting surface area available for the process [38–41].

For both reactants, the change from amorphous to the anatase structure is verified by Raman spectra, as seen in Figure 5. Thereby, for deposition temperatures below 250 and 300°C for H_2O and O_3, respectively, layers show mainly

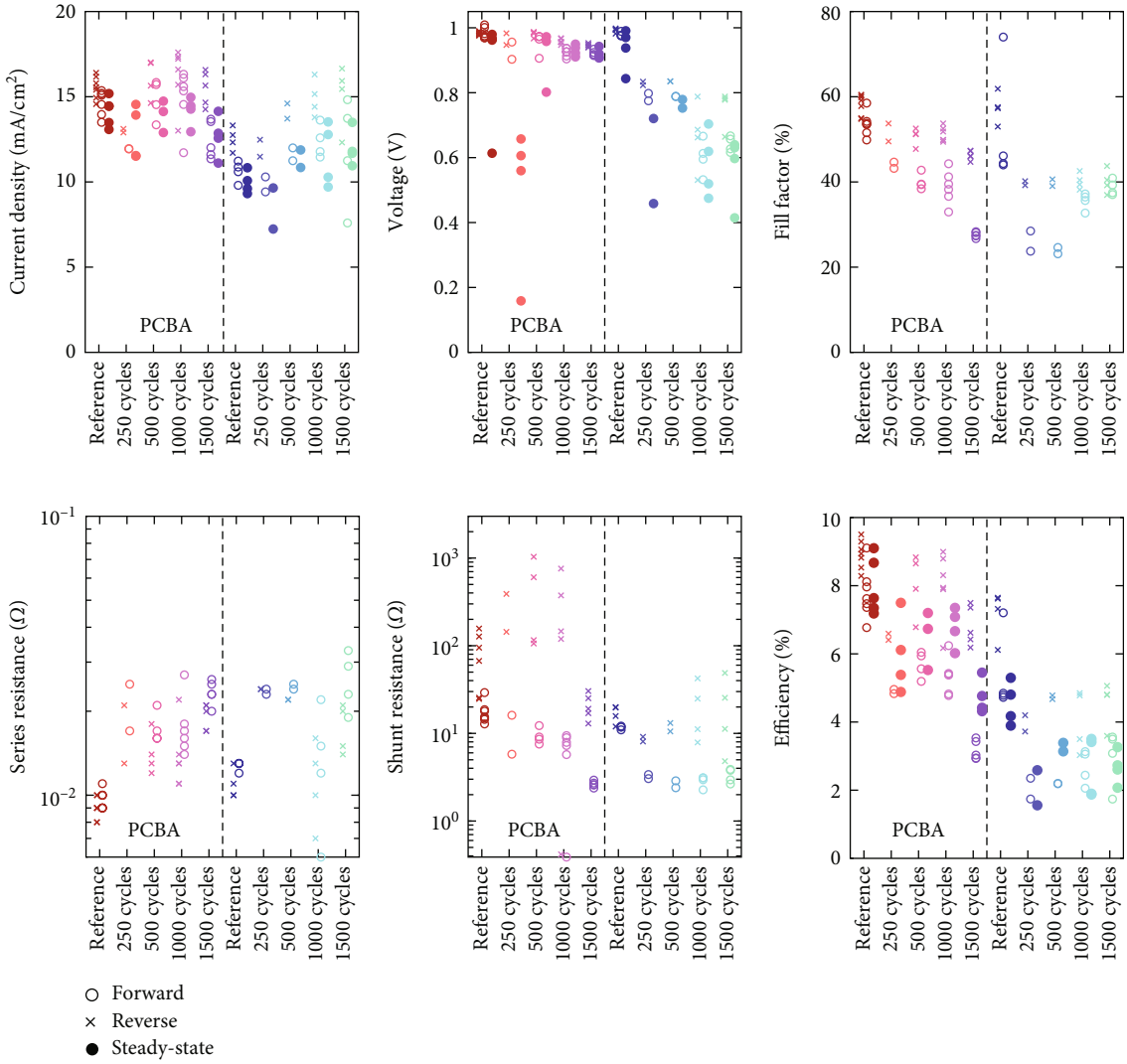

Figure 6: Thickness dependent solar cell characteristics for PCBA modified (left) and unmodified (right) SALD layers fabricated at 200°C. Reference layer were fabricated with a commercial sol-gel. Solar cells have been measured in forward (open circle), reverse (x), and under steady state conditions (filled circle). The different panels show the J_{SC}, V_{OC}, Fill factor (FF), R_{series}, R_{Sh}, and the power conversion efficiency, respectively.

amorphous character. For higher temperatures, detected peak positions correspond to literature values of anatase at 144, 196, 397, 513/519, and 639 cm^{-1}, whereas rutile signals at 143, 447, 612, or 826 cm^{-1} are not observable [42, 43]. The significant increase in Raman intensity with higher temperature is attributed to an increasing crystallinity as indicated from SEM images in Figure 3. This is also consistent with EDX measurements showing a raise in the atomic percentage of titanium and oxygen relative to the silicon substrate for increasing temperatures (see Figure S18 and Table S1 in the SI) due to an increase in layer density. Thereby, the atomic percentage of Ti is increasing linearly from 4.5 to 10% for H_2O starting at deposition temperatures of 100°C, whereas for O_3 the values only start to rise above 200°C. This goes along with a decrease of the O : Ti ratio from about 3.5 to 2.8, assuming the contribution by a native SiO_2 layer on the Si substrate to be insignificant.

We note that intensities in Raman and EDX are sensitive to variations in layer density and thickness. However, the relatively small variation in layer thickness does not explain the significant increase of the Raman intensity towards higher process temperatures. In addition, XPS, which is not thickness-dependent, also shows increased signal intensities while the C 1s peak is not systematically affected (see Figure 2). Hence, the change of atomic percentage is attributed to an increased packing density due to enhanced crystallinity. Table 1 is summarizing relevant properties extracted from structural and optoelectronic measurement techniques.

3.2. Optical and Electronic Analysis. Optical and electronic properties were investigated by UPS, KP, UV-Vis, SE, and in terms of solar cells. The corresponding measurements are shown in Figures S19 and S20 (UPS), Figure S21 (UV-Vis), and Figures S22 and S23 (SE) in the SI.

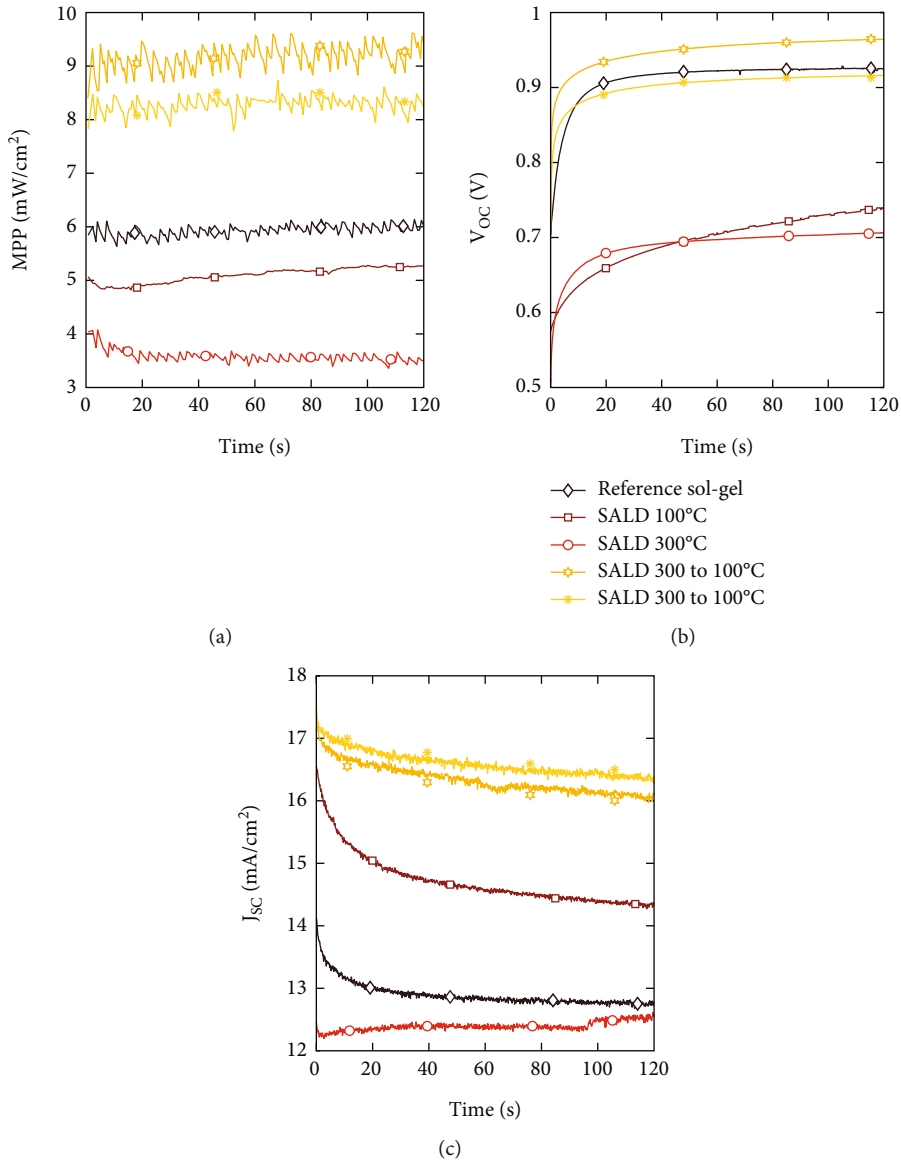

FIGURE 7: Steady state device characteristics of solar cells fabricated on TiO_2 deposited with 1000 cycles at 100°C, 300°C, and with a gradient from 300°C to 100°C (the latter for two different batches of devices with high reproducibility). Sol-gel-based TiO_2 solar cell as reference. All devices without PCBA modification: (a) maximum power-point (MPP), (b) V_{OC}, and c) J_{SC} tracking over time.

From UPS and KP measurements, the work function (WF) and valence band maximum (VBM) were determined at energies of about −4.6 eV and −7.5 eV, respectively. In combination with the optical bandgap determined from UV-Vis, the conduction band minimum of fabricated TiO_2 layers is located at an energy of about −3.9 to −4.0 eV and therefore the Fermi level is steadily 0.7 eV below the conduction band. The corresponding measurements are presented in Table 1 and Figure S24 in the SI.

Meanwhile, the optical bandgap and the extinction coefficient are consistently shifting to lower energies with increasing deposition temperatures as expected for an increasing crystallinity [8], and the change in crystallinity results in a significant increase in refractive index from about 2.07 to 2.54 and 2.57 at 530 nm for H_2O and O_3, respectively. This has to be considered for light propagation and standing wave formation within solar cell devices, which can modulate the resulting short circuit current density (J_{SC}) [44, 45].

The influence of varying TiO_2 properties on solar cell characteristics was exemplarily inspected on perovskite-based solar cells ($MAPbI_3$, 2-step process) utilizing AP-SALD layers with the most promising conditions or variations. Fabricated devices have been compared to a commercial sol-gel reference without further optimization (see Figure 6), yielding flat, at about 70 nm thick compact layers with a surface roughness and morphology comparable to amorphous AP-SALD layers fabricated at temperatures of 200°C and below. More detailed device characteristics of fabricated solar cells are shown in Figures S25 to S30 in the SI.

Compared to the reference sample prepared with commercial TiO_2 paste, the series resistance is higher and shunt resistance is lower in AP-SALD-based solar cells, which is directly reflected in a decreased fill factor. The slightly higher series resistance is attributed to the complete absence of unintentional doping and a more stoichiometric TiO_2 crystal formation with less oxygen vacancies during deposition. These vacancies are known to be responsible for the intrinsic conductivity of TiO_2 [46]. The decreased shunt resistance, on the other hand, is attributed to the TiO_2 interface of as-processed layers to the perovskite. The absence of dopants and impurities within the bulk and at the surface of the fabricated layers presumably leads to an unfavorable energy landscape for electron extraction, which was already observed for TiO_2 and other metal oxides [47–49]. Thus, a surface passivation by PCBA strongly enhanced open circuit voltage (V_{OC}) and fill factor of fabricated devices.

However, this impact of the interface is strongly interfering with a direct association of layer properties to device characteristics. Thus, in spite of significant changes in layer properties like layer thickness, morphology, crystallinity, and stoichiometry, clear systematic dependencies of device characteristics were largely superimposed and are mainly within our given uncertainty of device reproducibility.

Common strategies for interface passivation are the application of very thin organic [50–52] or inorganic [53, 54] interface layers which are improving charge extraction and avoiding recombination. Also, ultrathin ALD layers of amorphous TiO_2 have been shown to act as suitable passivation layer [55].

Integrating this approach into the AP-SALD deposition by a continuous gradual change of temperature allows for an uninterrupted fabrication process of the TiO_2, reducing complexity and avoiding a possible contamination of the surface between fabrication steps. Therefore, we investigated the influence of temperature gradients during deposition and compared them to layers deposited at fixed temperatures. For layers fabricated with a temperature gradient from 300 to 100°C we find a significant improvement in all device characteristics (see Figure 7) and attribute this to the formation of a core-shell structure with an amorphous layer covering a crystalline anatase film. This combines the good series resistance of the crystalline phase with an improved interface avoiding recombination [56].

4. Conclusion

The analysis of structural and optoelectronical characterization methods shows a significant influence of temperature and the chosen reactant on crystallinity and grain size of deposited AP-SALD layers. Thereby, low deposition temperatures result in smooth amorphous TiO_2 films, while elevated temperatures lead to polycrystalline anatase layers. With increasing deposition temperature, the preferential crystal growth is increasing the resulting surface area and roughness. Simultaneously, the improving crystallinity leads to a higher refractive index and lower optical band gap, though the energy levels of the layer are only slightly altered. In fabricated perovskite-based solar cells, the impact of an unfavorable interface restricts a clear association of TiO_2 layer to specific changes in device characteristics and highlights once again the necessity of adequate interface engineering. Thus, a promising approach for gradual core-shell structures was demonstrated, leading to an amorphous passivation layer on top of highly crystalline anatase TiO_2 for improved solar cells.

Data Availability

Data of this work are available on reasonable request.

Conflicts of Interest

The authors declare that they have no known competing financial interests or personal relationships that could have appeared to influence the work reported in this paper.

Acknowledgments

The authors would like to thank Karl-Philipp Strunk for conducting Kelvin-Probe measurements at the University of Heidelberg. The authors would also like to thank Mikhail Fonin for granting access to the XPS/UPS System and Marina Krumova for taking the TEM and SAD images. We acknowledge the funding from the German Research Foundation (DFG), the German Federal Ministry of Education and Research (BMBF, project MesoPIN), the Baden-Württemberg Foundation for the project "BioMat-S7: SUPERSOL" in the program "Biomimetic Materials Synthesis", and the REFINE research consortium funded by the Carl Zeiss Foundation.

Supplementary Materials

In the supplementary information we supply details on the applied methods for the TiO_2 preparation, perovskite solar cells preparation, applied measurement techniques, and more data for the structural analysis. Figure S1: layer thickness as a function of (a) deposition cycles and (b) temperature measured by profilometer, and (c) growth per cycle determined by VASE. Layers in (a) and (b) are fabricated with H_2O as reactant, whereas GPC was determined for H_2O and O_2 as reactant. Figure S2: XPS overview and detailed scans of TiO_2 with H_2O as reactant at varying deposition temperatures. Figure S3: XPS overview and detailed scans of TiO_2 with O_3 as reactant at varying deposition temperatures. Figure S4: XPS overview and detailed scans of TiO_2 with H_2O as reactant comparing a layer with 75 deposition cycles to a layer with 1000 deposition cycles. Figure S5: SEM (InLens detector) of 1000 cycles SALD with H_2O as reactant at 100°C. Figure S6: SEM (InLens detector) of 1000 cycles SALD with H_2O as reactant at 150°C. Figure S7: SEM (InLens detector) of 1000 cycles SALD with H_2O as reactant at 200°C. Figure S8: SEM (InLens detector) of 1000 cycles SALD with H_2O as reactant at 250°C. Figure S9: SEM (InLens detector) of 1000 cycles SALD with H_2O as reactant at 300°C. Figure S10: SEM (InLens detector) of 1000 cycles SALD with H_2O as reactant at 350°C. Figure

S11: SEM (InLens detector) of 1000 cycles SALD with O_3 as reactant at 100°C. Figure S12: SEM (InLens detector) of 1000 cycles SALD with O_3 as reactant at 150°C. Figure S13: SEM (InLens detector) of 1000 cycles SALD with O_3 as reactant at 200°C. Figure S14: SEM (InLens detector) of 1000 cycles SALD with O_3 as reactant at 250°C. Figure S15: SEM (InLens detector) of 1000 cycles SALD with O_3 as reactant at 300°C. Figure S16: SEM (InLens detector) of 1000 cycles SALD with O_3 as reactant at 350°C. Figure S17: AFM of 1000 cycles SALD on polished Si at varying deposition temperatures and reactants. Figure S18: atomic percent of Ti, Si, and O of 1000 cycles SALD at varying temperatures measured by EDX. Figure S19: UPS of TiO_2 fabricated with 1000 cycles and H_2O as reactant at varying temperatures. Figure S20: UPS of TiO_2 fabricated with 1000 cycles and O_3 as reactant at varying temperatures. Figure S21: transmission spectra acquired by UV-Vis spectroscopy for TiO_2 layers fabricated with (a) H_2O and (b) O_3 as reactant at varying deposition temperatures. Layer thickness and refractive index show a significant impact on standing-wave formation, while crystallinity is causing a shift in energy bandgap to lower energies. We note that measured absolute bandgap values of anatase are slightly higher than commonly reported in literature. Figure S22: dispersion relation of refractive index and extinction coefficient of TiO_2 deposited at varying temperatures and H_2O as reactant. Figure S23: dispersion relation of refractive index and extinction coefficient of TiO_2 deposited at varying temperatures and O_3 as reactant. Figure S24: work function, valence band maximum, and conduction band minimum as a function of temperature measured by Kelvin probe, UPS, and UV-Vis. Figure S25: thickness dependent solar cell characteristics for SALD layers fabricated at 200°C and partially modified with PCBA. Figure S26: steady state measurement of solar cells presented in Figure S25. Figure S27: thickness and deposition temperature dependent solar cell characteristics for SALD layers modified with PCBA. Figure S28: steady state measurement of solar cells presented in Figure S27. Figure S29: solar cell characteristics for SALD layers fabricated at fixed and gradient temperatures, modified with PCBA. Figure S30: steady state measurement of solar cells presented in Figure S29. Figure S31: SEM (InLens detector) of 1000 cycles SALD with H2O as reactant for a continuous temperature gradient from 300 to 100°C. *(Supplementary Materials)*

References

[1] F. D. Hardcastle, H. Ishihara, R. Sharma, and A. S. Biris, "Photoelectroactivity and Raman spectroscopy of anodized titania (TiO_2) photoactive water-splitting catalysts as a function of oxygen-annealing temperature," *Journal of Materials Chemistry*, vol. 21, no. 17, p. 6337, 2011.

[2] M. Ferroni, V. Guidi, G. Martinelli, G. Faglia, P. Nelli, and G. Sberveglieri, "Characterization of a nanosized TiO_2 gas sensor," *Nanostructured Materials*, vol. 7, no. 7, pp. 709–718, 1996.

[3] C. Garzella, E. Comini, E. Tempesti, C. Frigeri, and G. Sberveglieri, "TiO_2 thin films by a novel sol–gel processing for gas sensor applications," *Sensors and Actuators B: Chemical*, vol. 68, no. 1-3, pp. 189–196, 2000.

[4] L. A. Majewski, R. Schroeder, and M. Grell, "Low-voltage, high-performance organic field-effect transistors with an ultra-thin TiO_2 layer as gate insulator," *Advanced Functional Materials*, vol. 15, no. 6, pp. 1017–1022, 2005.

[5] P. H. Wöbkenberg, T. Ishwara, J. Nelson, D. D. C. Bradley, S. A. Haque, and T. D. Anthopoulos, "TiO_2 thin-film transistors fabricated by spray pyrolysis," *Physics Letters*, vol. 96, no. 8, article 082116, 2010.

[6] W. S. Shih, S. J. Young, L. W. Ji, W. Water, and H. W. Shiu, "TiO_2-based thin film transistors with amorphous and anatase channel layer," *Journal of the Electrochemical Society*, vol. 158, no. 6, article H609, 2011.

[7] B. O'Regan and M. Gratzel, "A low-cost, high-efficiency solar cell based on dye-sensitized colloidal TiO_2 films," *Nature*, vol. 353, no. 6346, pp. 737–740, 1991.

[8] M. K. Bera and C. K. Maiti, "Charge trapping properties of ultra-thin TiO_2 films on strained-Si," *Semiconductor Science and Technology*, vol. 22, no. 7, pp. 774–783, 2007.

[9] L. Forro, O. Chauvet, D. Emin, L. Zuppiroli, H. Berger, and F. Lévy, "High mobilityn-type charge carriers in large single crystals of anatase (TiO_2)," *Journal of Applied Physics*, vol. 75, no. 1, pp. 633–635, 1994.

[10] W. W. Xu, R. Kershaw, K. Dwight, and A. Wold, "Preparation and characterization of TiO_2 films by a novel spray pyrolysis method," *Materials Research Bulletin*, vol. 25, no. 11, pp. 1385–1392, 1990.

[11] M. O. Abou-Helal and W. T. Seeber, "Preparation of TiO_2 thin films by spray pyrolysis to be used as a photocatalyst," *Applied Surface Science*, vol. 195, no. 1-4, pp. 53–62, 2002.

[12] M. Okuya, K. Nakade, and S. Kaneko, "Porous TiO_2 thin films synthesized by a spray pyrolysis deposition (SPD) technique and their application to dye-sensitized solar cells," *Solar Energy Materials & Solar Cells*, vol. 70, no. 4, pp. 425–435, 2002.

[13] W. D. Sproul, M. E. Graham, M.-S. Wong, and P. J. Rudnik, "Reactive d.c. magnetron sputtering of the oxides of Ti, Zr, and Hf," *Surface and Coatings Technology*, vol. 89, no. 1-2, pp. 10–15, 1997.

[14] K. N. Rao, M. A. Murthy, and S. Mohan, "Optical properties of electron-beam-evaporated TiO_2 films," *Thin Solid Films*, vol. 176, no. 2, pp. 181–186, 1989.

[15] Q. Zhang and G. L. Griffin, "Gas-phase kinetics for TiO_2 CVD: hot-wall reactor results," *Thin Solid Films*, vol. 263, no. 1, pp. 65–71, 1995.

[16] B. G. Dixon, M. A. Walsh, P. G. Phillips, and R. Scott Morris, "Generation of amorphous ceramic capacitor coatings on titanium using a continuous sol-gel process," *Journal of Materials Research*, vol. 10, no. 10, article 2626, 1995.

[17] S. D. Burnside, V. Shklover, C. Barbé et al., "Self-organization of TiO_2 nanoparticles in thin films," *Chemistry of Materials*, vol. 10, no. 9, pp. 2419–2425, 1998.

[18] C.-C. Wang and J. Y. Ying, "Sol–gel synthesis and hydrothermal processing of anatase and rutile titania nanocrystals," *Chemistry of Materials*, vol. 11, no. 11, pp. 3113–3120, 1999.

[19] S. Karuppuchamy, D. P. Amalnerkar, K. Yamaguchi, T. Yoshida, T. Sugiura, and H. Minoura, "Cathodic electrodeposition of TiO_2 thin films for dye-sensitized photoelectrochemical applications," *Chemistry Letters*, vol. 30, no. 1, pp. 78-79, 2001.

[20] Y. Ishikawa and Y. Matsumoto, "Electrodeposition of TiO_2 photocatalyst into nano-pores of hard alumite," *Electrochimica Acta*, vol. 46, no. 18, pp. 2819–2824, 2001.

[21] L. Kavan, M. Kalbáč, M. Zukalová et al., "Lithium storage in nanostructured TiO_2 made by hydrothermal growth," *Chemistry of Materials*, vol. 16, no. 3, pp. 477–485, 2004.

[22] C. J. Barbé, F. Arendse, P. Comte et al., "Nanocrystalline titanium oxide electrodes for photovoltaic applications," *Journal of the American Ceramic Society*, vol. 80, no. 12, pp. 3157–3171, 1997.

[23] J. Aarik, A. Aidla, T. Uustare, and V. Sammelselg, "Morphology and structure of TiO_2 thin films grown by atomic layer deposition," *Journal of Crystal Growth*, vol. 148, no. 3, pp. 268–275, 1995.

[24] J. Aarik, A. Aidla, T. Uustare, M. Ritala, and M. Leskelä, "Titanium isopropoxide as a precursor for atomic layer deposition: characterization of titanium dioxide growth process," *Applied Surface Science*, vol. 161, no. 3-4, pp. 385–395, 2000.

[25] L. Aarik, T. Arroval, R. Rammula, H. Mändar, V. Sammelselg, and J. Aarik, "Atomic layer deposition of TiO_2 from $TiCl_4$ and O_3," *Thin Solid Films*, vol. 542, pp. 100–107, 2013.

[26] S. Zhuiykov, M. K. Akbari, Z. Hai, C. Xue, H. Xu, and L. Hyde, "Wafer-scale fabrication of conformal atomic-layered TiO_2 by atomic layer deposition using tetrakis (dimethylamino) titanium and H_2O precursors," *Materials & Design*, vol. 120, pp. 99–108, 2017.

[27] D. Muñoz-Rojas and J. MacManus-Driscoll, "Spatial atmospheric atomic layer deposition: a new laboratory and industrial tool for low-cost photovoltaics," *Materials Horizons*, vol. 1, no. 3, pp. 314–320, 2014.

[28] D. Muñoz-Rojas, H. Sun, D. C. Iza et al., "High-speed atmospheric atomic layer deposition of ultra thin amorphous TiO_2 blocking layers at 100 °C for inverted bulk heterojunction solar cells," *Progress in Photovoltaics: Research and Applications*, vol. 21, no. 4, pp. 393–400, 2013.

[29] J. T. Mayer, U. Diebold, T. E. Madey, and E. Garfunkel, "Titanium and reduced titania overlayers on titanium dioxide (110)," *Journal of Electron Spectroscopy and Related Phenomena*, vol. 73, no. 1, pp. 1–11, 1995.

[30] U. Diebold and T. E. Madey, "TiO_2 by XPS," *Surface Science Spectra*, vol. 4, no. 3, pp. 227–231, 1996.

[31] V. V. Atuchin, V. G. Kesler, N. V. Pervukhina, and Z. Zhang, "Ti 2p and O 1s core levels and chemical bonding in titanium-bearing oxides," *Journal of Electron Spectroscopy and Related Phenomena*, vol. 152, no. 1-2, pp. 18–24, 2006.

[32] I. Iatsunskyi, M. Kempiński, G. Nowaczyk et al., "Structural and XPS studies of PSi/TiO_2 nanocomposites prepared by ALD and Ag-assisted chemical etching," *Applied Surface Science*, vol. 347, pp. 777–783, 2015.

[33] I. I. Kabir, L. R. Sheppard, R. Shamiri et al., "Contamination of TiO_2 thin films spin coated on borosilicate and rutile substrates," *Journal of Materials Science*, vol. 55, no. 9, pp. 3774–3794, 2020.

[34] I. Kavre Piltaver, R. Peter, I. Šarić et al., "Controlling the grain size of polycrystalline TiO_2 films grown by atomic layer deposition," *Surface Science*, vol. 419, pp. 564–572, 2017.

[35] G. Luka, B. S. Witkowski, L. Wachnicki, M. Andrzejczuk, M. Lewandowska, and M. Godlewski, "Kinetics of anatase phase formation in TiO_2 films during atomic layer deposition and post-deposition annealing," *CrystEngComm*, vol. 15, no. 46, p. 9949, 2013.

[36] C. Armstrong, L. V. Delumeau, D. Munoz-Rojas, A. Kursumovic, J. MacManus-Driscoll, and K. P. Musselman, "Tuning the band gap and carrier concentration of titania films grown by spatial atomic layer deposition: a precursor comparison," *Nanoscale Advances*, vol. 3, no. 20, pp. 5908–5918, 2021.

[37] W.-J. Lee and M.-H. Hon, "Space-limited crystal growth mechanism of TiO_2 films by atomic layer deposition," *Journal of Physical Chemistry C*, vol. 114, no. 15, pp. 6917–6921, 2010.

[38] O. Bondarchuk, Y. K. Kim, J. M. White, J. Kim, B. D. Kay, and Z. Dohnalek, "Surface chemistry of 2-propanol on TiO_2(110): - low- and high-temperature dehydration, isotope effects, and influence of local surface structure," *Journal of Physical Chemistry C*, vol. 111, no. 29, pp. 11059–11067, 2007.

[39] R. A. Hackler, G. Kang, G. C. Schatz, P. C. Stair, and R. P. Van Duyne, "Analysis of tio_2 atomic layer deposition surface chemistry and evidence of propene oligomerization using surface-enhanced Raman spectroscopy," *Journal of the American Chemical Society*, vol. 141, no. 1, pp. 414–422, 2019.

[40] V. R. Rai and S. Agarwal, "Surface reaction mechanisms during ozone-based atomic layer deposition of titanium dioxide," *Journal of Physical Chemistry C*, vol. 112, no. 26, pp. 9552–9554, 2008.

[41] J. P. Klesko, R. Rahman, A. Dangerfield et al., "Selective atomic layer deposition mechanism for titanium dioxide films with (EtCp)Ti(NMe2)3: ozone versus water," *Chemistry of Materials*, vol. 30, no. 3, pp. 970–981, 2018.

[42] P. P. Lottici, D. Bersani, M. Braghini, and A. Montenero, "Raman scattering characterization of gel-derived titania glass," *Journal of Materials Science*, vol. 28, no. 1, pp. 177–183, 1993.

[43] S. Sahoo, A. K. Arora, and V. Sridharan, "Raman line shapes of optical phonons of different symmetries in anatase TiO_2 nanocrystals," *Journal of Physical Chemistry C*, vol. 113, no. 39, pp. 16927–16933, 2009.

[44] G. F. Burkhard, E. T. Hoke, and M. D. McGehee, "Accounting for interference, scattering, and electrode absorption to make accurate internal quantum efficiency measurements in organic and other thin solar cells," *Advanced Materials*, vol. 22, no. 30, pp. 3293–3297, 2010.

[45] K. D. Kim, T. Pfadler, E. Zimmermann et al., "Decoupling optical and electronic optimization of organic solar cells using high-performance temperature-stable $TiO_2/Ag/TiO_2$ electrodes," *APL Materials*, vol. 3, no. 10, article 106105, 2015.

[46] A. Folger, J. Kalb, L. Schmidt-Mende, and C. Scheu, "Tuning the Electronic Conductivity in Hydrothermally Grown Rutile TiO_2 Nanowires: Effect of Heat Treatment in Different Environments," *Nanomaterials (Basel)*, vol. 7, no. 10, p. 289, 2017.

[47] Y. Lee, S. Lee, G. Seo et al., "Efficient planar perovskite solar cells using passivated tin oxide as an electron transport layer," *Advanced Science (Weinh)*, vol. 5, no. 6, p. 1800130, 2018.

[48] L. Zuo, Z. Gu, T. Ye et al., "Enhanced photovoltaic performance of CH3NH3PbI3 perovskite solar cells through interfacial engineering using self-assembling monolayer," *Journal of the American Chemical Society*, vol. 137, no. 7, pp. 2674–2679, 2015.

[49] Y.-N. Zhang, B. Li, L.-Y. Zhang, and L.-W. Yin, "Efficient electron transfer layer based on Al_2O_3 passivated TiO_2 nanorod arrays for high performance evaporation-route deposited FAPbI3 perovskite solar cells," *Solar Energy Materials & Solar Cells*, vol. 170, pp. 187–196, 2017.

[50] J. Cao, J. Yin, S. Yuan, Y. Zhao, J. Li, and N. Zheng, "Thiols as interfacial modifiers to enhance the performance and stability of perovskite solar cells," *Nanoscale*, vol. 7, no. 21, pp. 9443–9447, 2015.

[51] L. Liu, A. Mei, T. Liu et al., "Fully printable mesoscopic perovskite solar cells with organic silane self-assembled monolayer," *Journal of the American Chemical Society*, vol. 137, no. 5, pp. 1790–1793, 2015.

[52] K. K. Wong, A. Fakharuddin, P. Ehrenreich et al., "Interface-dependent radiative and nonradiative recombination in perovskite solar cells," *Journal of Physical Chemistry C*, vol. 122, no. 20, pp. 10691–10698, 2018.

[53] S. Ito, S. Tanaka, K. Manabe, and H. Nishino, "Effects of surface blocking layer of Sb_2S_3 on nanocrystalline TiO2 for CH3NH3PbI3 perovskite solar cells," *Journal of Physical Chemistry C*, vol. 118, no. 30, pp. 16995–17000, 2014.

[54] T. C. Li, M. S. Góes, F. Fabregat-Santiago et al., "Surface passivation of nanoporous TiO_2 via atomic layer deposition of ZrO_2 for solid-state dye-sensitized solar cell applications," *Journal of Physical Chemistry C*, vol. 113, no. 42, pp. 18385–18390, 2009.

[55] S. S. Mali, C. S. Shim, H. K. Park, J. Heo, P. S. Patil, and C. K. Hong, "Ultrathin atomic layer deposited TiO_2 for surface passivation of hydrothermally grown 1D TiO_2 nanorod arrays for efficient solid-state perovskite solar cells," *Chemistry of Materials*, vol. 27, no. 5, pp. 1541–1551, 2015.

[56] J. A. Dorman, J. Weickert, J. B. Reindl et al., "Control of recombination pathways in TiO_2 nanowire hybrid solar cells using Sn_4+ dopants," *Journal of Physical Chemistry C*, vol. 118, no. 30, pp. 16672–16679, 2014.